PERSEE, the dynamic nulling demonstrator: Recent progress on the cophasing system

Houairi K.[a,b,c], Cassaing F. [a,c], Le Duigou J.M. [b], Sorrente B. [a,c],
Jacquinod S.[d], Amans J.P. [e,c]

[a]Office National d'Etudes et de Recherche Aérospatiales, Optics Department, BP 72, 92322 Châtillon Cedex, France;
[b]Centre National d'Etudes Spatiales, 18 Avenue Edouard Belin, 31401 Toulouse Cedex 4, France;
[c]PHASE, the high angular resolution partnership between Onera, Observatoire de Paris, CNRS and University Denis Diderot Paris 7;
[d] Institut d'Astrophysique Spatiale, Centre universitaire d'Orsay, Bt 120-121, 91405 Orsay, France;
[e]GEPI, UMR 8111, Observatoire de Paris, 5 place Jules Janssen, 92190 Meudon, France;

ABSTRACT

Spectral characterization of exo-planets can be made by nulling interferometers. In this context, several projects have been proposed such as DARWIN, FKSI, PEGASE and TPF, space-based, and ALADDIN, ground-based. To stabilize the beams with the required nanometric accuracy, a cophasing system is required, made of piston/tip/tilt actuators on each arm and piston/tip-tilt sensors. The demonstration of the feasibility of such a cophasing system is a central issue.

In this goal, a laboratory breadboard named PERSEE is under integration. Main goals of PERSEE are the demonstration of a polychromatic null from 1.65 µm to 3.3 µm with a 10^{-4} rejection rate and a 10^{-5} stability despite the introduction of realistic perturbations, the study of the interfaces with formation-flying spacecrafts and the joint operation of the cophasing system with the nuller.

We describe the principle of the cophasing system made by Onera, operating in the $[0.8-1]$ µm (tip/tilt) and $[0.8-1.5]$ µm (piston) spectral bands. Emphasis is put on the piston sensor and its close integration with the nuller.

Keywords: Interferometry, nulling, Persee, Pegase, fringe tracking, ground demonstration

1. INTRODUCTION

Nulling interferometry is one of the most promising methods to make spectral characterisation of exoplanets and to study habitable extrasolar systems. In the last few years, several projects have been proposed such as DARWIN,[1,2] FKSI,[3] PEGASE[4] and TPF,[5,6] space-based, and ALADDIN,[7] ground-based. These projects are based on the Bracewell interferometric principle[8] which is made technologically possible thanks to the ability of measuring and correcting the optical path difference (OPD) between the beams. This principle requires a control of the OPD with an accuracy of a few nanometers despite the perturbations during the exposure time mainly arising from the mechanical motions of the spacecrafts (space-based interferometers) or from the atmospheric turbulence (ground-based interferometers). The requirement for this OPD stability cannot be met without a cophasing system.

A laboratory breadboard called PERSEE,[9] of which goal is to show the feasibility of such missions, is under integration. PERSEE is built by a consortium including CNES, IAS, LESIA, OCA, Onera and TAS. Its main goals are the demonstration of a polychromatic null with a 10^{-4} rejection rate and a 10^{-5} stability despite the introduction of realistic perturbations, the study of the interfaces with the formation-fying spacecrafts and the

E-mail: kamel.houairi@onera.fr

joint operation of the cophasing system with the nuller.[10] The broadboard integration and performance tests should end in 2009.

We list the operating modes of the cophasing system of PERSEE, its different estimators and its current status.

2. FRINGE TRACKING SPECIFICATIONS

One of the main requirements of the cophasing system is the minimization of differential paths with the science channel. A Modified Mach-Zehnder interferometer[11] allows the minimization of the differential aberrations by joining the measurement and the science channels. PERSEE's Modified Mach-Zehnder interferometer is fully described in Ref. [10].

PERSEE's cophasing system is implemented within two parallel servo loops: the OPD control loop and the tip/tilt control loop These fine loops compensate the external movements by corresponding displacements of optical delay lines and fast steering mirrors. The fringe sensor (FS) operates in the [0.8-1.5] µm spectral band while the star tracker system camera operates in the [0.8-1] µm.[9] The optical elements which perform the corrections are detailed in Ref. [9]. Both these servo loops are implemented in a real time computer which derives the corrections from the data.

The specifications and the preliminary test results of the tip/tilt control loop are presented in Ref. [9] and in the following we focus on the OPD control loop. In order to reach an average null depth of 10^{-4} with a 10^{-5} stability, the residual OPD must be lower than 2 nm rms. To reach this specification, two correction levels are implemented: a centimetric level correcting with an accuracy of about one micron and a nanometric level correction with an accuracy of 0.2 nm.

The fringe tracker operates within three modes: the fringe detection mode during which we see the fringes for the first time, the fringe acquisition mode during which the central dark fringe is located, and the tracking mode during which the science channel makes observations. These different operating modes are detailed in the following.

2.1 Detection mode

The first step of interferometers is the fringe detection. Indeed, the fringes are only present when the optical path difference between the two beams is lower than one coherence length of the fringe sensor. In formation flying space-based interferometers, because of the mechanical drift of the spacecrafts, we can wait for detecting them. An other considered solution is to scan the fringes by moving the delay lines.

When the visibility of the fringes is higher than a threshold, a real time computer derives the fringe position, their visibility, drift speed and drift direction. In Pegase context, because of the large size of the interferometer baseline ([50-500] m), the speed v of the fringes can reach several hundreds of µm/s. Consequently, to avoid blurring, the exposure time of the FS must be close to 1 ms, and the repetition time small enough so that measurements correctly sample the chromatic envelope of the fringe pattern, of which coherence length is a few microns. The fringe tracker must be capable of detecting fringes with a speed up to 150 µm/s.

When the fringes are detected and the delay lines are actioned, the fringe tracker automatically changes into *acquisition mode*.

2.2 Acquisition mode

At the beginning of the acquisition phase, the OPD between the two beams can be much larger than the FS operating wavelength. The goal of this phase is to locate the central dark fringe and to make the OPD between the two beams be lower than the FS operating wavelength. To do so, the fringe sensor spectral band is dispersed into 2 spectral channels.

When the OPD residual is lower than a fraction of the FS operating wavelength, the fringe tracker automatically changes into *tracking mode*.

2.3 Tracking mode

The tracking phase is the period during which the fringes are stabilized and the science channel makes observations. The main requirement is that the residual OPD must be lower than 2 nm rms. To reach this specification, it has been specified that the phase tracking must be performed with a sampling rate be close to 1 kHz.

At last, in case of fringe jumps, the dispersion will ensure the dark fringe tracking by removing the main ambiguities.

3. DESIGN OF THE FRINGE SENSOR

3.1 Selected concept

In order to minimize the differential aberrations between the fringe sensor and the scientific channel, the same modified Mach-Zehnder is used for the OPD measurement channel and the nulling channel.[10] This spectral separation carried out by dichroic plates located after the interferometric combination allows to measure OPD in the spectral band $[0.8-1.5]$ µm while the null depth is computed in several spectral channels in $[1.65-3.3]$ µm. The demodulation is carried out by the ABCD algorithm, the $\{0-\pi/2-\pi-3\pi/2\}$ modulation is performed by adding a $\pi/2$ phase-shift in the MMZ.

At last, the real time computering is carried out by the software LabVieW Real Time in a PXI chassis.

3.2 Estimators

Each fringe tracking mode needs specific estimators. The main estimator of each mode are:

- *Mode detection*: visibility
- *Mode acquisition*: group delay
- *Mode tracking*: phase delay

The main difference between the coherencing phase and the cophasing phase is the measurable OPD: it is lower than the beat wavelength, λ_B, during the coherencing and it is lower than the shortest measurement wavelength, λ_I, during the cophasing. The beat wavelength λ_B is defined by:

$$\lambda_B = \frac{\lambda_I \lambda_J}{\lambda_J - \lambda_I} \tag{1}$$

where λ_I and λ_J are the FS operating wavelengths ($\lambda_I < \lambda_J$). Since the spectral band $[0.8-1.5]$ µm is dispersed into 2 spectral channels, we call I the first spectral channel and J the second one.

For each FS operating mode, we need to find the best estimator, i.e. the one of which the measurement is performed with the highest accuracy.

3.2.1 Fringe visibility

In order to detect the fringes , the chosen estimator is the effective square fringe visibility $\widehat{W}$:

$$\widehat{W} = \widehat{V'^2} \tag{2}$$

where the real visibility $\widehat{V'}$ takes into account the dynamical loss caused by the fringe blurring arising from the fringe drift during the exposure time and the static loss caused by the chromatic envelope of the fringe pattern when the OPD is not zero. For instance, as long as the OPD is lower than half the coherence length L_c, the static loss is lower than 1/2. Thus, the real visibility $\widehat{V'}$ can be written as:

$$\widehat{V'} = V \,\mathrm{sinc}\left(\frac{vT_p}{\lambda}\right) \mathrm{Env}\left(\frac{\delta}{L_c}\right) \tag{3}$$

where T_p is the integration time, δ is the OPD, v the fringe drift speed and λ the measurement wavelength. The fringe envelope Env is the inverse Fourier Transform absolute value of the FS spectrum and the function $sinc$ is the Fourier Transform of the rectangular function:

$$\mathrm{sinc}\,(x) = \frac{\sin(\pi x)}{\pi x} \tag{4}$$

Since the visibility is estimated over each spectral channel, instead of averaging the visibility measurement of each spectral channel, we balance the measurement thanks to a coefficient q and we define the estimated fringe visibility as:

$$\widehat{W} = q\widehat{W_I} + (1-q)\widehat{W_J} \tag{5}$$

Thus, during the detection phase, the signal-to-noise ratio of the main estimator is:

$$SNR_{vis} = \frac{q\widehat{W_I} + (1-q)\widehat{W_J}}{\sqrt{q^2\sigma^2_{\widehat{W_I}} + (1-q)^2\sigma^2_{\widehat{W_J}}}} \tag{6}$$

We see how to choose the coefficient q in section 3.3.

3.2.2 Coherencing

One coherencing estimator which allows to identify without any ambiguity the central dark fringe is:

$$\widehat{\Phi} = \widehat{\varphi_I} - \widehat{\varphi_J} \tag{7}$$

and considering that the phase measurements $\widehat{\varphi_I}$ and $\widehat{\varphi_J}$ in each spectral channel I and J are decorrelated, the variance of the estimated phase $\widehat{\Phi}$ can be written as:

$$\sigma^2_{\widehat{\Phi}} = \sigma^2_{\widehat{\varphi_I}} + \sigma^2_{\widehat{\varphi_J}} \tag{8}$$

The measurement of the phase for a pairwise combination of 2 beams a and b is corrupted according to Refs. (12–14):

$$\sigma_{\widehat{\varphi}} = \frac{1}{V^*_{a,b}} \times \frac{\alpha}{\eta_{a,b}\rho_{a,b}} \tag{9}$$

where α is a coefficient depending on the chosen combination (co-axial or multi-axial) and demodulation algorithm. The source visibility $V^*_{a,b}$ takes into account the instrumental contrast loss and the fluctuation of the output, $\eta_{a,b}$ is the contrast attenuation factor introduced by the photometric imbalance and $\rho_{a,b}$ is the photometric signal-to-noise ratio. One can write:

$$\eta_{a,b} = \frac{2\sqrt{N_a N_b}}{N_a + N_b} \qquad \text{and} \qquad \rho_{a,b} = \frac{N_a + N_b}{\sqrt{(N_a + N_b) + K\sigma_d^2}} \tag{10}$$

where N_a (respectively N_b) is the number of photoelectrons detected during the exposure time onto the detector a (respectively b), σ_d is the detector noise and K is the number of pixels read ($K = 4$ for the ABCD algorithm).

3.2.3 Cophasing

During the fringe tracking, we can use only the phase measurement $\widehat{\varphi_I}$ or only the phase measurement $\widehat{\varphi_J}$ or even the two phase average. However, we balance the two phase measurements thanks to a coefficient p in order to take more or less into account the measurement of $\widehat{\varphi_I}$ or $\widehat{\varphi_J}$. Indeed, both $\widehat{\varphi_I}$ and $\widehat{\varphi_J}$ provide $\widehat{\varphi}$ but they are more or less corrupted by noise. Thus, we define the estimated phase as:

$$\widehat{\varphi} = p\widehat{\varphi_I} + (1-p)\widehat{\varphi_J} \tag{11}$$

Assuming that the phase measurements $\widehat{\varphi_I}$ and $\widehat{\varphi_J}$ are decorrelated, the variance of the estimated phase $\widehat{\varphi}$ can be written as:

$$\sigma^2_{\widehat{\varphi}} = p^2\sigma^2_{\widehat{\varphi_I}} + (1-p)^2\sigma^2_{\widehat{\varphi}_J} \tag{12}$$

We see how to choose the coefficient p in section 3.3.

3.2.4 Fringe drift speed

We assume that between two measurements, the fringes drift with a constant speed. A fringe drift speed estimator can be derived from two succesive coherencing phase measurements $\widehat{\Phi}$, at instants t_1 and t_2 ($\tau = t_2 - t_1$).

$$\widehat{v} = \frac{\widehat{\Phi}(t_2) - \widehat{\Phi}(t_1)}{\tau} \tag{13}$$

Considering the two measurements decorrelated, the variance of the fringe drift speed measurement noise can be written as:

$$\sigma_v^2 = 2\frac{\sigma_\Phi^2}{\tau^2} \tag{14}$$

The minimization of the fringe drift speed measurement noise is the same as the one for the coherencing.

3.3 Optimization of the spectral channels

For the following simulations, we assume that we are photon-noise limited and we simplified the calculations by assuming that the source spectrum is gaussian over the each spectral band with a full width at half maximum equal to the coherence wavelength L_c. We illustrate the spectrum of the source in each spectral channel in Fig. 1.

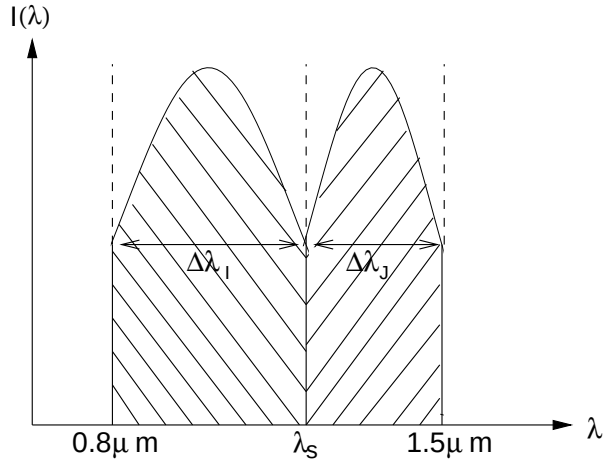

Figure 1. Spectrum of each spectral channel

Both spectra have the same maximum intensity spectral density. We performed other simulations by changing the maximum value of the intensity spectral density in each spectral band and the same results are obtained as far as their ratio is lower than a few dozens.

3.3.1 Visibility

According to Ref. 12, when the OPD is much higher than the coherence length, the visibility noise standard deviation for a ABCD algorithm is:

$$\sigma_W = \frac{4}{N} \tag{15}$$

where N is the number of photoelectrons detected during the exposure time.

From Eq. (6) and (15), for each splitting wavelength λ_s, we optimize SNR_{vis} by choosing the coefficient q which maximizes SNR_{vis}. In figure 2 we plot the optimized relative SNR_{vis} versus the splitting wavelength λ_s.

SNR_{vis} depends on the splitting wavelength λ_s but is not very sensitive. Indeed, when $\lambda_s \in [0.8 - 1.5]$ μm, SNR_{vis} evolution is lower than 30%. The splitting wavelength which maximizes the signal-to-noise ratio during the detection phase is $\lambda_s = 0.9$ μm.

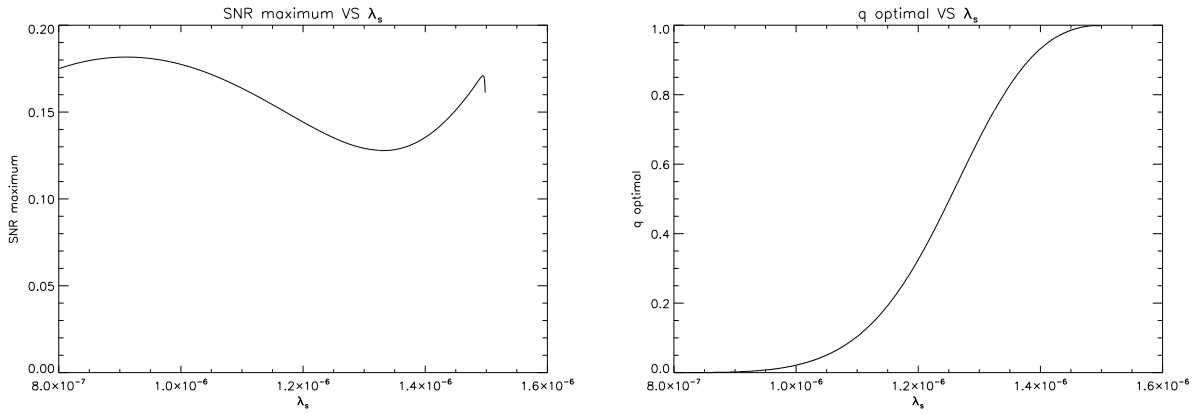

Maximum SNR_{vis} optimal q

Figure 2. Visibility SNR vs λ_s

3.3.2 Group delay

From Eq. (8-10), we derive the standard deviation of the relative phase measurement noise versus the splitting wavelength λ_s. It is plotted in Fig. 3

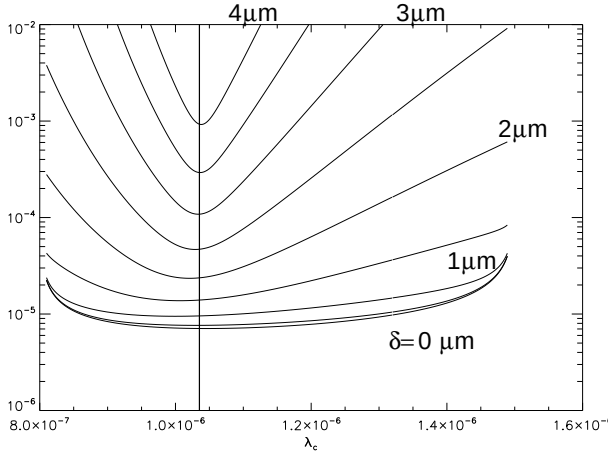

Figure 3. Phase measurement noise standard deviation during the coherencing phase.

σ_φ strongly depends on the splitting wavelength λ_s. According to Fig. 3, the splitting wavelength which minimizes the phase measurement noise during the acquisition phase is $\lambda_s = 1.03$ µm.

3.3.3 Phase delay

Combining Eqs. (9), (10) and (12) and according to the considered spectrum in each spectral channel shown in Fig. 1, for each splitting wavelength λ_s we optimize $\sigma_{\widehat{\varphi}}$ by choosing the coefficient p which minimizes $\sigma_{\widehat{\varphi}}$. In figure 2 we plot the optimized relative $\sigma_{\widehat{\varphi}}$ versus the splitting wavelength λ_s.

According to Fig. 3, the splitting wavelength which minimizes the phase measurement noise during the tracking phase is $\lambda_s = 1.03$ µm.

3.3.4 Coherence length

We show in Fig. 5 the coherence length of each spectral channel versus the splitting wavelength λ_s.

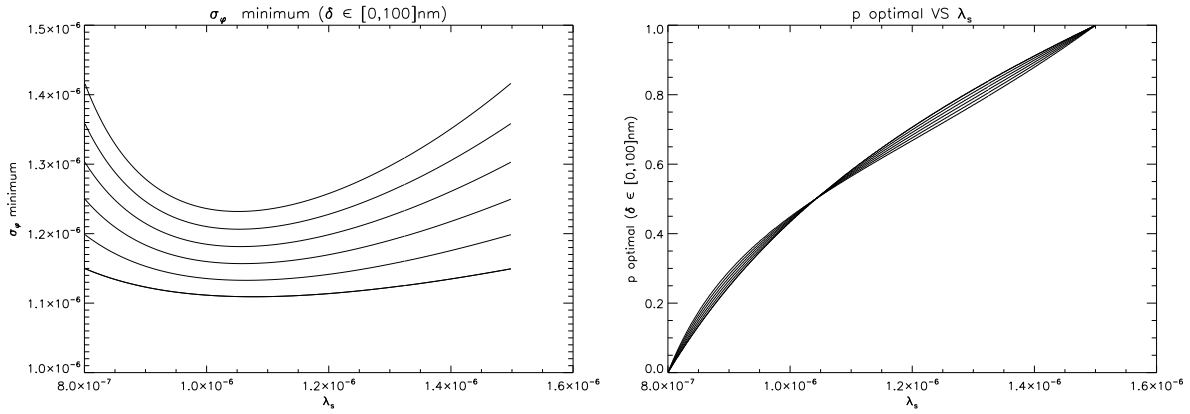

Phase delay - Measurement noise Phase delay - optimal p

Figure 4. Phase measurement noise evolution functions of OPD ($\delta = 0 - 20 - 40 - 60 - 80 - 100\ nm$) versus λ_s during the cophasing phase.

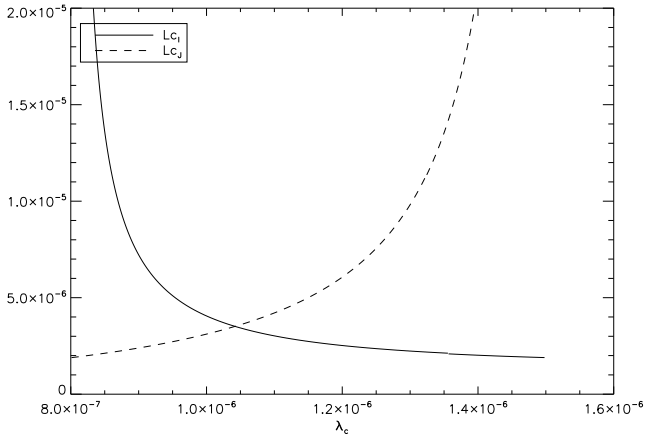

Figure 5. Coherence length of each spectral channel.

Coherencing and cophasing phases are not optimized when channels have similar width $\Delta\lambda$ but when they have similar coherence length L_c. Indeed, for this splitting wavelength, the measurement noise of each spectral channel is well-balanced.

4. IMPLENTATION OF THE FRINGE SENSOR

By waiting for the final integration of PERSEE at *Observatoire de Paris-Meudon* in 2009, fringe tracking tests will be performed at Onera. Figure 6 shows the principle of the cophasing loop tests at Onera.

At Onera, with a reduced setup at Onera in autocollimation, the light will be injected through an output of the MMZ which will thus be used both in order to divide and to recombine the beams as shown in Figure 6. The sources used for the tests at Onera will be a distributed feedback laser at 830 nm and a amplified spontaneous emission at 1310 nm with a 75 nm full width at half maximum.

Since the Modified-Mach-Zehnder described in Ref. 10 is not manufactured yet. The tests of the cophasing loop will be carried out with a priliminary MMZ manufactured by GEPI. It has been specially designed in order to reach the thermal stability requirement. GEPI has also manufactured two injection blocs shown in Figure 6: 4 dichroic plates disperse the input beams in the [0.8-1] µm and [1-1.5] µm spectral channels and 4 lenses focus the beams into the 8 monopixel detectors.

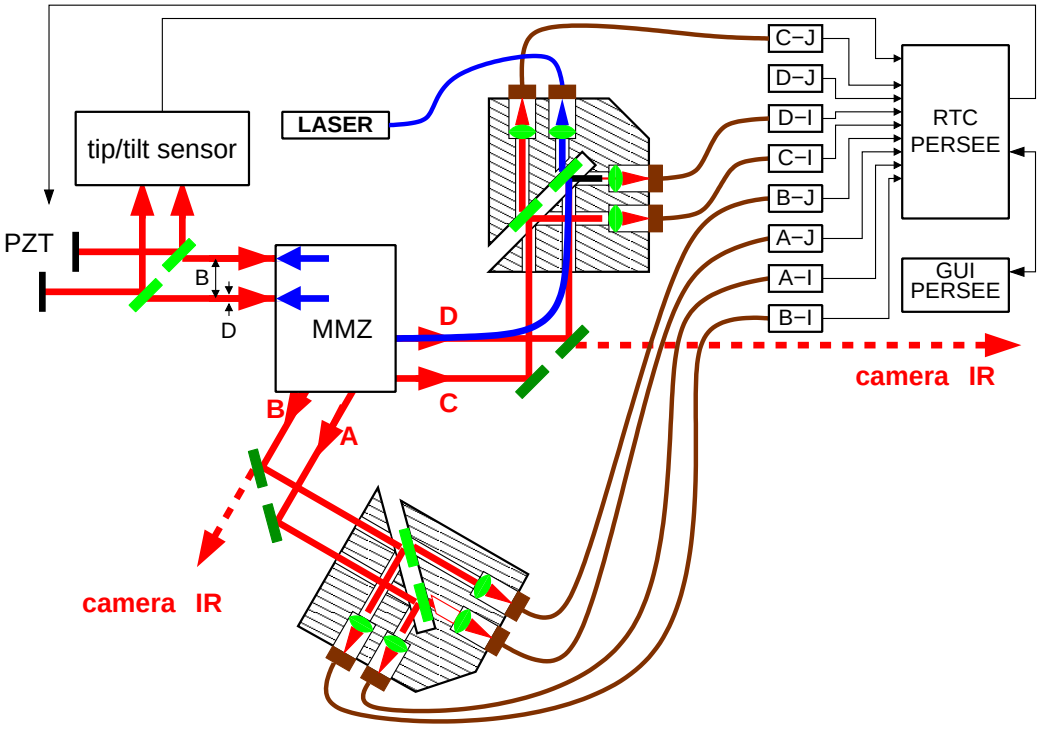

Figure 6. Principle of the cophasing loop tests at Onera.

For the tests at Onera, the same piezoelectric actuators will perform the correction of the star tracking and fringe tracking systems. They will then be also used for simulating perturbations in piston and tip/tilt.

5. STATUS OF THE FRINGE SENSOR

The components of the fringe sensor have been specified. The computer hardware is available and the software is under integration. All the optomechanics as well as optics components are now at Onera. Detector tests and the alignment of the MMZ are ongoing. The integration and the tests of the fringe tracking system will be carried out in summer 2008.

The priliminary integration of the cophasing loop at Onera will allow the optimization of the estimators and calibration procedure. Fringe tracking performance should reach the OPD residuals specification of 2 nm rms.

6. CONCLUSION

In order to obtain a polychromatic null with a 10^{-4} rejection rate and a 10^{-5} stability, a high-performance cophasing system with OPD residuals lower than 2 nm rms is required. PERSEE's fringe tracking best goal is to obtain OPD residuals lower than 1 nm rms.

The stringent requirement of the fringe tracking system led to the development of an innovative fringe tracking system where the fringe sensor is implemented in the science instrument in order to minimize the differential aberrations. So that the fringe sensor identifies the central dark fringe without any ambiguity, the flux is dispersed over two spectral channels which have been optimized with respect to the measurement accuracy. Also, the chosen setup allows the fringe sensor to measure in real time the null depth: it would thus be possible to calibrate in real time the differential aberrations between the measurement and the science channels which could arise from temperature change. The loop will be closed with a sampling frequency close to 1 kHz.

The performance of the fringe tracking system will allow bottom-up specifications for formation flying missions by specifying the maximum tolerable satellite perturbations.

REFERENCES

[1] Leger, A. and Herbst, T., "DARWIN mission proposal to ESA," *ArXiv e-prints* **707** (July 2007).

[2] Cockell, C. S., Leger, A., Fridlund, M., Herbst, T., Kaltenegger, L., Absil, O., Beichman, C., Benz, W., Blanc, M., Brack, A., Chelli, A., Colangeli, L., Cottin, H., Coude du Foresto, V., Danchi, W., Defrere, D., den Herder, J. ., Eiroa, C., Greaves, J., Henning, T., Johnston, K., Jones, H., Labadie, L., Lammer, H., Launhardt, R., Lawson, P., Lay, O. P., LeDuigou, J. ., Liseau, R., Malbet, F., Martin, S. R., Mawet, D., Mourard, D., Moutou, C., Mugnier, L., Paresce, F., Quirrenbach, A., Rabbia, Y., Raven, J. A., Rottgering, H. J. A., Rouan, D., Santos, N., Selsis, F., Serabyn, E., Shibai, H., Tamura, M., Thiebaut, E., Westall, F., White, and Glenn, J., "DARWIN - A Mission to Detect, and Search for Life on, Extrasolar Planets," *ArXiv e-prints* **805** (May 2008).

[3] Danchi, W. C., Barry, R. K., Deming, D., Kuchner, M., Monnier, J. D., Mundy, L. G., Rajagopal, J., Richardson, J., Seager, S., and Traub, W., "Scientific rationale for exoplanet characterization from 3-8 microns: the FKSI mission," in [*Advances in Stellar Interferometry. Edited by Monnier, John D.; Schöller, Markus; Danchi, William C.. Proceedings of the SPIE, Volume 6268, pp. 626820 (2006).*], *Presented at the Society of Photo-Optical Instrumentation Engineers (SPIE) Conference* **6268** (July 2006).

[4] Ollivier et al., M., "Pegase, an infrared interferometer to study stellar environments and low mass companions around nearby stars," *ESA's Cosmic Vision Call for Proposals* (2007).

[5] Lawson, P. R., Dumont, P. J., and Colavita, M. M., "Interferometer Designs for the Terrestrial Planet Finder," in [*Bulletin of the American Astronomical Society*], *Bulletin of the American Astronomical Society* **31**, 835–+ (May 1999).

[6] Beichman, C., Lawson, P., Lay, O., Ahmed, A., Unwin, S., and Johnston, K., "Status of the terrestrial planet finder interferometer (TPF-I)," in [*Advances in Stellar Interferometry. Edited by Monnier, John D.; Schöller, Markus; Danchi, William C.. Proceedings of the SPIE, Volume 6268, pp. 62680S (2006).*], *Presented at the Society of Photo-Optical Instrumentation Engineers (SPIE) Conference* **6268** (July 2006).

[7] Coudé du Foresto, V., Absil, O., Swain, M., Vakili, F., and Barillot, M., "ALADDIN: an optimized nulling ground-based demonstrator for DARWIN," in [*Advances in Stellar Interferometry. Edited by Monnier, John D.; Schöller, Markus; Danchi, William C.. Proceedings of the SPIE, Volume 6268, pp. 626810 (2006).*], *Presented at the Society of Photo-Optical Instrumentation Engineers (SPIE) Conference* **6268** (July 2006).

[8] Bracewell, R. N., "Detecting nonsolar planets by spinning infrared interferometer," *Nature* **274**, 780–+ (Aug. 1978).

[9] Cassaing, F., Duigou, J.-M. L., Houairi, K., Jacquinod, S., Reess, J.-M., Henault, F., Sorrente, B., Barillot, M., Rousset, G., du Foresto, V. C., and Ollivier, M., "Persee: a nulling demonstrator with real-time correction of external disturbances," in [*Optical and Infrared Interferometry*], Danchi, W. C., Delplancke, F., and Schller, M., eds., **7013** (2008).

[10] Jacquinod, S., Cassaing, F., Duigou, J.-M. L., Barillot, M., Ollivier, M., Houairi, K., and Amans, J.-P., "PERSEE: description of a new concept for nulling interferometry recombination and opd measurement," in [*Optical and Infrared Interferometry*], Danchi, W. C., Delplancke, F., and Schller, M., eds., **7013** (2008).

[11] Serabyn, E. and Colavita, M. M., "Fully symmetric nulling beam combiners," *Appl. Opt.* **40**(10), 1668–1671 (2001).

[12] Shao, M., Colavita, M. M., Hines, B. E., Staelin, D. H., and Hutter, D. J., "The Mark III stellar interferometer," *Astronomy and Astrophysics* **193**, 357–371 (Mar. 1988).

[13] Surrel, Y., "Additive noise effect in digital phase detection," *Appl. Opt.* **36**, 271–275 (Jan. 1997).

[14] Cassaing, F., "Optical path difference sensors," in [*Comptes Rendus de l'Académie des Sciences*], *IV Physics*, 1–12 (2001).